Effect of Mn Doping on The Structural, Optical, Magnetic Properties and Antibacterial Activity of ZnO Nanospheres

EBENEZAR JEYASINGH (ebey_ebenezar@yahoo.com)
Jamal Mohamed College https://orcid.org/0000-0001-7391-5429
Kelvin Adaikalam Charles
Jamal Mohamed College
Pandiyarajan Thangaraj
Indian Institute of Information Technology Design and Manufacturing Kurnool
Karthikeyan Chandrasekaran
Centro de Investigación de Polímeros Avanzados: Centro de Investigacion de Polimeros Avanzados
Mangalaraja Ramalinga Viswanathan
University of Concepción: Universidad de Concepcion

Original Research

Keywords: Mn doped ZnO, Co-precipitation method, Luminescence, Antibacterial activity, Magnetic property

Posted Date: February 10th, 2021

DOI: https://doi.org/10.21203/rs.3.rs-173208/v1

Version of Record: A version of this preprint was published at Journal of Sol-Gel Science and Technology on April 6th, 2022. See the published version at https://doi.org/10.1007/s10971-022-05778-0.

Effect of Mn doping on the structural, optical, magnetic properties and antibacterial activity of ZnO nanospheres

Ebenezar Jeyasingh[1*], Kelvin Adaikalam Charles[1†], Pandiyarajan Thangaraj[2, 3], Karthikeyan Chandrasekaran[4] and Mangalaraja Ramalinga Viswanathan[2,5]

[1]PG & Research Department of Physics, Jamal Mohamed College (Autonomous), Tiruchirappalli – 620020, INDIA.

[2]Department of Materials Engineering, University of Concepcion, Concepcion, CHILE.

[3]Department of Sciences, Indian Institute of Information Technology, Design and Manufacturing, Kurnool, Andhra Pradesh, India.

[4]Centro de Investigacion de Polimeros Avanzados (CIPA), Concepcion, CHILE.

[4]Technological Development Unit (UDT), University of Concepcion, Coronel Industrial Park, Coronel, CHILE.

[†]Present Address: Department of Physics, K. Ramakrishnan College of Engineering, Tiruchirappalli – 621112, INDIA.

[*]**Corresponding authors:**

Dr. Ebenezar Jeyasingh
Assistant Professor
PG & Research Department of Physics,
Jamal Mohamed College (Autonomous),
Tiruchirappalli – 620020,
INDIA.
E-mail: ebey_ebenezar@yahoo.com

Abstract

In this work, a systematic study of structural, optical, magnetic and antibacterial properties of Mn doped ZnO has been investigated. Zinc oxide (ZnO) and Mn^{2+} doped zinc oxide (ZnMnO) nanoparticles (NPs) were prepared through co-precipitation method. The X-ray diffraction studies confirmed that the synthesize nanoparticles did not modify the crystal structure upon Mn doping, but the microstructural parameters were changed considerably while increasing the concentration of Mn dopant. The HRTEM images showed that the ZnO NPs were exhibited nanospheres like morphology and a reduction in the average particle size from 41 nm to 33 nm were observed upon Mn^{2+} doping. The elemental composition of Zn, Mn and O atoms were identified by EDAX spectra. The Zn-O stretching bands were observed at 539 and 525cm^{-1} in the FTIR spectra and, the zinc and oxygen vacancies defects were confirmed by PL spectra. From the UV-Vis spectra, the band gap was estimated as 2.7 eV for pure and 2.9 eV for Mn doped ZnO NPs. The Mn doped ZnO NPs showed greater antibacterial effect than the pure ZnO NPs. The magnetization measurements for Mn doped ZnO samples under room temperature ferromagnetism (RTFM) showed the ferromagnetic phase that could originated from the interactions between Mn^{2+} ions and oxygen vacancies and the defects incorporated in the ZnO matrix.

Keywords: Mn doped ZnO; Co-precipitation method; Luminescence; Antibacterial activity; Magnetic property.

1. Introduction

With the rapid development of nanotechnology, a diverse range of nanomaterials and nanoproducts are emerging [1]. ZnO nanoparticles, as one common engineered nanomaterial, have used in various technological field such as sunscreen products, textiles, paintings, industrial coatings, and antimicrobial agents [2, 3]. The II-VI semiconductor ZnO NPs possess the large exciton binding energy of 60 meV and direct band gap (3.36 eV) at room temperature, which have the promising applications in the optoelectronics and photonics [4-7]. The synthesis of the size and shape of the metal oxide nanostructures is significant role in controlling their physical and chemical properties for their potential application. Size of the materials becomes smaller; the band gap becomes larger, thereby changing the optical and electrical properties of the material. As a result of these changes, it is now possible to develop newer applications and devices using these materials. The modification of electrical and optical properties of a semiconductor is the generally accepted methods and it's the addition of impurity atoms or doping [8-10]. In early literature, the synthesis of ZnO and doped ZnO nanoparticles, this can be characterized into either chemical or physical method [11,12], hydrothermal process [13], sol-gel method [14] and co-precipitation method [15]. Among these method of co-precipitation is suitable and preferred methods to prepare the nanoparticles. Cetin et al., (2012) reported that magnesium doped ZnO nanofibers has increased the band gap [16] and calcium doping in ZnO NPs has relaxed strain in the unit cell [17].

The antibacterial activity of ZnO NPs can be widely studied [18-21]. Commonly accepted mechanism of antibacterial action is the material production of reactive oxygen species (ROS) [22] on the surface of these NPs in the light causes oxidative stresses in bacterial cells and leads to the cell death. ROS contain the most reactive hydroxyl radical

(OH), less toxic superoxide anion radical (O^{2-}) and hydrogen peroxide with a weaker oxidizer (H_2O_2). This can damage DNA, cell membranes etc., leading to cell death [23]. It is suggested that both ZnO NPs and Zn^{2+} are toxic but have different modes of action taking place in the antibacterial cell death. In the present investigation, pure and Mn^{2+} doped ZnO NPs are synthesized by co-precipitation method and prepared nanoparticles characterized by structural, optical, magnetic and antibacterial properties.

2. Experimental

2.1 Material synthesis

All chemicals were analytically pure and used without additional purification. The anhydrous pure zinc acetate and Sodium hydroxide of Merck Company is used. Zinc acetate [$Zn(CH_3COO)_2.2H_2O$], was used as zinc sources, which provide the zinc ion for the reaction.

A chemical co-precipitation method was employed to synthesis pure and Mn doped ZnO NPs in colloidal solution. The synthesis was used in a zinc acetate and sodium hydroxide solution in which manganese acetate [$Mn(CH_3COO)_2.2H_2O$], was added as doping agents. For pure ZnO, 2.19 g of zinc acetate [0.1M] was dissolved in 100 ml of distilled water and 3.2 g of sodium hydroxide was dissolved in 100 ml of distilled water. Then NaOH solution of 3.2 g was added drop by drop into zinc acetate dehydrate solution until the solution reaches the white milky precipitates. The white colour precipitate was called as the zinc oxide solution. Then centrifuge the solution for 5 min at 3000 rpm by repeating the process for 5 times and washed it with distilled water. The final precipitates were collected to maintain at the temperature of 90 $^{\circ}$C for 4 to 5 hrs, to get a white coloured solid powder form of ZnO.

Mn doped ZnO nanoparticles were prepared as follows: 0.024 g (1%) 0.049 g (2%) and 0.073 g (3%) of manganese acetate was added to 100 ml of distilled water to get the Mn solution separately, and then each solution was added to zinc acetate solution of 2.17 g, 2.15 g and

2.12 g respectively. Then NaOH solution of 3.2 g was added drop wise in the above each solution; it formed a dark brown precipitate. The procedure for the precipitation of undoped ZnO NPs was adopted for the preparation of Mn doped ZnO nanoparticles. The precipitates appeared as black coloured Mn doped ZnO samples. Finally, obtained samples were annealed at 700 $^{\circ}$C for 2 hrs for the energy from the heat can enhance the vibration and diffusion of lattice atoms for crystallization. The annealed nanopowder of ZnO will be used for further studies. The prepared pure and Mn doped ZnO samples were code named as ZnO, ZnMnO1, ZnMnO2 and ZnMnO for 0%, 1%, 2% and 3% of Mn concentrations, respectively.

1.2 Instrumentation

The ZnO NPs were characterized by using X-ray diffractometer (XRD model: X'PERT PRO PANalytical) for their structural analysis. The diffraction patterns were recorded in the range of 20^{o} – 80^{o} for the ZnO samples where the monochromatic wavelength of 1.54 $\AA$ was used. The morphology of the synthesized ZnO was examined by using high-resolution transmission electron microscopy (HRTEM). The copper grid was finally dried at room temperature and was subjected to HRTEM analysis by the instrument Tecnai F20 model operated at an accelerating voltage of 200 kV. The elemental composition was done using an energy dispersive X-ray spectroscopy (EDAX model: AMETEK) with FEI-QUANDA 200F HRSEM operated at 30 kV. FT-IR spectra were recorded by using Perkin-Elmer spectrometer through KBr pellet technique. The UV-Vis-NIR spectrum documented in the wavelength range 190 – 1110 nm by using Lambda 35. The photoluminescence (PL) measurement was performed on a spectrofluorometer (FLUROLOG-3-11, HORIBA Jobin Yvon, USA) at the excitation wavelength of 330 nm.

2.3 Testing of antibacterial activity

The bacterial activity is frequently tested using a disk diffusion test**,** by using antibiotic filled disks (Kirby-Bauer). A related test with nanoparticle laden disks was used in

this study. 3.8 g of Muller Hinton Agar (MHA) powder was dissolved in 100 ml of water by gently boiling in a conical flask. The agar solution was sterilized by autoclaving at 15 lbs pressure at 121°C for 15 min. Then it was cooled to 40-45 °C in a laminar hood, which was disinfected beforehand following the same method as described earlier. Nearly 20 mL of the above medium was added into all sterilized petri-dishes, separately after taking all precautions to avoid any contamination. The dishes were cooled for sufficient time (25-35 min) to solidify the agar medium, then a sterile cotton swab was used to inoculate the culture on surface of Muller Hinton Agar plate rotating the plate every 60°C to ensure homogeneous growth. The nanoparticle coated disks (6 mm diameter) were placed in each dish were made by sterilized forceps. 20 μL of test solution of different concentrations were poured in each disk in two dishes. Each such dish contained two different concentrations (0.6 mg and 1.20 mg) of ZnO, ZnMnO1 (1%), ZnMnO2 (2%) & ZnMnO3 (3%) NPs and the dishes were rapped well by a paraffin film to seal them. The entire handling was done inside the laminar hood in front of the flame of a spirit lamp. The plates were incubated at 35°C for 24 hrs and the inhibition zone was measured. The mean reported for each concentration of nanoparticle and with each microbial strain were based on three replicates. Methicillin was used as positive control. All the media and disk were purchased from Hi-Media (Mumbai, India).

3. Results and Discussion

3.1 XRD analysis

Fig. 1 shows the XRD patterns of pure ZnO and 1%, 2%, 3% Mn doped ZnO NPs. Patterns show strong and sharp peaks at (100), (002), (101) planes which confirm the wurtzite hexagonal structure of ZnO (hexagonal phase and space group $p6_3$ mc) with lattice constants of a = b = 3.249 Å and c = 5.206 Å corresponding to JCPDS card No. 36-1451. The peaks are located at the angle (2θ) of 31.8°, 34.4°, 36.3°, which correspond to (100), (002), (101) planes of the ZnO; Similarly, other peaks are found in the (2θ) angles of 47.4°, 56.7°, 62.9°,

66.2°, 68.0°, 69.2°, 72.4° and 77.3°, corresponding to (102), (110), (103), (200), (112), (201), (004) and (202) planes of the wurtzite structure, respectively. Interesting Mn doped samples show no secondary peaks, which confirm there is no secondary phase formation, but there is a slight lower angle shift compared to undoped ZnO NPs diffraction pattern and further the intensities are decreased with increasing the concentration of Mn.

Particle size determination:

The particle size of the pure and Mn doped ZnO can be calculated using Debey-Scherer's formula:

$$D = \frac{k\lambda}{\beta_{hkl}\cos\theta}$$

where the constant k is the shape factor = 0.94, λ is the wavelength of *X*-rays (1.5418 for Cu $K\alpha$), θ is Bragg's angle, β is the full width at the half- maximum (FWHM). The particle size of the pure ZnO was calculated as 41.6 nm and when the dopant manganese was added to pure ZnO, the crystallite size of the NPs gets decreased to 40.1 and 33.8 nm for ZnMnO2 and ZnMnO3, respectively. Staumal et al. [24] investigated that the decrease of crystallite size is due to increase of Mn solubility in ZnO. However, in all the Mn doped samples, the particle size gets reduced gradually with increasing of Mn concentration [Table 2].

The lattice parameters of ZnO nanostructures are highly depend on the doping concentrations since there is difference of dopant ionic radius with respect to the ZnO matrix.

$$\frac{1}{d_{hkl}^2} = \frac{4}{3}\left(\frac{h^2+hk+k^2}{a^2}\right) + \frac{l^2}{c^2}$$

with the first order approximation (n=1) for the (100) plane the lattice constant 'a' is obtained through the relation $a = \frac{\lambda}{\sqrt{3}\sin\theta}$ and the lattice constant 'c' can be derived for the plane

(002) by the relation $c = \frac{\lambda}{\sin\theta}$ and unit cell volume could be deduced from the formulae [25] $v = \frac{\sqrt{3}a^2 c}{2}$. The dopant induced change in the bond length was deduced from the relation [26] $L = \sqrt{\left(\frac{a^2}{3}\right) + \left(\frac{1}{2} - u_p\right)^2 c^2}$ where, 'a', and 'c' are lattice parameters and 'u_p' is the positional parameter which can be calculated by the formula $u_p = \left(\frac{a^2}{3c^2}\right) + 0.25$. The calculated lattice constants and bond length is shown in Fig. 2a and b. It shows an increase in lattice constant due to Mn doping. The lattice constants of Mn doped ZnO were more than that of undoped ZnO, because of the ionic radius of Mn^{2+} (0.66 Å) is larger than that of Zn^{2+} (0.74 Å) [27].

The dopant induced lattice strain can be extracted from the peak broadening of diffraction line. The peak broadening of diffraction line is due to the combination of lattice strain and the particle size with respect to diffraction angle and it can be written as $\beta_{hkl} = \beta_t + \beta_e$ [28] where β_t is line broadening due to the particle size and β_e is due to the strain induced by dopant ions. The particle size could be evaluated by using the Scherrer formula and peak broadening due to strain can be calculated $\beta_e = 4\varepsilon \tan\theta$ where ε is the microstrain. The peak broadening due to the combination of particle size as well as microstrain can be written mathematically [29] $\beta_{hkl}\cos\theta_{hkl} = \frac{k\lambda}{D} + 4\varepsilon \sin\theta$. The microstarin was extracted from the plot of $\beta_{hkl}\cos\theta_{hkl}$ vs $4\sin\theta$ (Fig. 3a). The variation in the microstarin upon Mn concentration is plotted and shown in Figure 3b. The results revealed that the up to 2% of Mn concentration, the microstrain is decreased with respect to the pure ZnO and increases for 3% of Mn concentration. This is due to lattice mismatch when the concentration of Mn is large [30].

3.2 HRTEM studies

The ordered lattice fringes in the HRTEM image further confirmed the single crystalline nature of pure ZnO and Mn doped ZnO NPs. Fig. 4.1 (a-d) shows the distribution of spherical shaped pure ZnO NPs. Fig. 4.2 (a-d) it's seen that images found from the portion of an individual ZnMnO particle confirms the better crystalline nature of ZnMnO NPs. Further, by the image analyzer software IMAGE-J on the lattice resolved TEM image, the distance between two parallel planes were observed at ~0.26 nm. Corresponding selected area electron diffraction (SAED) pattern of pure and manganese doped ZnO NPs is shown in Fig. 4.1 & 4.2 (a-d). The superimpositions of the bright spots indicate the good crystalline nature of the samples with equal lattice arrangement.

3.3 EDAX analysis

The EDAX spectra of the pure ZnO, ZnMnO1, ZnMnO2 and ZnMnO3 NPs are shown in Fig. 5 (a-d). From the EDAX spectra, the amounts of Zn, Mn, O atoms that present in the samples are given in Table 2. In the pure ZnO NPs, the chemical compositions of Zn and O were observed at 59.25 and 40.75% and for the doped ZnO NPs the Mn concentrations are 0.53, 1.04 and 1.91% for ZnMnO1, ZnMnO2 and ZnMnO3 NPs, respectively. Whereas, in the Mn doped ZnO NPs, the zinc percentage decreases with the increasing percentage of oxygen depending on the increasing doping concentrations.

3.4 UV spectroscopy analysis

The UV-Vis absorption spectra of the pure and Mn doped ZnO NPs samples were done by dispersing 3 mg of powder in 10 mL water and the spectrum is shown in Fig. 6. The absorbance is expected to depend on some factors like band gap, oxygen deficiency, surface roughness and impurity centres [27]. The absorbance spectra exhibit an absorption edges

around 350–380 nm, this is due to the photo-excitation of electrons from valence band to conduction band. The absorption edge of different samples slightly varies as the concentration of Mn in the ZnO nanoparticles fluctuates. The absorption edges of pure and 1, 2 and 3% Mn doped ZnO are 376, 374, 374 and 373 nm, respectively. The absorption edges position is to shift toward the lower wavelength side, with increasing the concentration of Mn doping in ZnO. The band gap of ZnO NPs increases with doping concentration of Mn ions and blue shift while doping ions in semiconductors, which can be described on the basis of the Burstein-Moss effect [30]. The blue shift may be attributed due to agglomeration in the sample [28-29].

3.4.1 Estimation of optical bandgap

The optical bandgap of the synthesized ZnO and Mn doped ZnO nanoparticles can be calculated using from this relation,

$$\alpha = 2.303 \frac{A}{t}$$

Where **A** is the absorbance and **t** is the thickness of the cuvette. The optical band gap of the NPs was determined by applying the Tauc relationship given by,

$$(h\upsilon\alpha)^{\frac{1}{n}} = A(h\upsilon - E_g)$$

Where **A** is a constant, **h** is Planck's constant, **υ** is the photon frequency, $\mathbf{E_g}$ is the optical band gap and **n=1/2** for direct bandgap semiconductor. An extrapolation of the linear region of a plot of $\mathbf{(\alpha h\upsilon)^2}$ on the Y- axis *vs.* Photon energy **(hυ)** on the X-axis gives the value of the optical band gap ($\mathbf{E_g}$).

The bandgap of undoped and Mn doped ZnO samples is measured by extrapolation of linear portion of the graph between the kublka-munk function $(h\upsilon\alpha)^2$ Vs $(h\upsilon)$ [27]. Fig. 7

shows the band gap energy diagram for pure and Mn doped ZnO nanoparticles. The calculated bandgap of pure ZnO nanoparticles was found to be 2.7 eV while in the case of Mn doped ZnO it was at 2.9 eV. The band gap energy of ZnO increases with the addition of Mn (except ZnMnO2). This is attributed to the increase in particle size of doped ZnO. It's clear that more level of doping (except ZnMnO2) causes an increase in the exitonic bandgap, proving the Burstein-Moss effect [26].

3.5 Photoluminescence (PL) analysis

Generally, the densities of defects and oxygen vacancies affect significantly the optical properties of oxide nanostructures. The correlation between structure and property is investigated by PL spectra of undoped and Mn doped ZnO nanoparticles excitation wavelength of 325 nm at room temperature is shown in Fig. 8. The PL spectra of the samples ZnO, ZnMnO1, ZnMnO2 and ZnMnO3 NPs demonstration a UV emission peak at ~387 to 397 nm and broad visible emission peaks including violet emission at ~416 to 418 nm, blue-green emission at ~480 to 479 nm and green emission at ~523 to 524 nm. The UV emission band is associated to near band-edge (NBE) emission of the ZnO NPs, and is due to the recombination of free excitons by exciton-exciton collision process [31, 32]. Several authors have investigated the PL properties of ZnO nanostructures [31–38]. Generally, visible emission in ZnO contains of blue, violet, green and yellow emission peaks, this may be ascribed to many intrinsic defects such as oxygen vacancies (V_o), zinc vacancies (V_{Zn}), oxygen interstitials (O_i), zinc interstitials (Zn_i) and oxygen antisites (O_{Zn}) [30]. UV peak is shifted from 394 to 387 nm with respect to the Mn concentrations (Fig. 8b), that shows the result is consistent with UV absorption spectra.

The violet emission in synthesized ZnO NPs centered at ~416 to ~418 nm is attributed to an electron transition from a shallow donor level of the neutral Zn_i to the top level of the

valence band [39]. A blue-green emission observed at ~480 to 479 nm is due to a radiative transition of an electron from the shallow donor level of Zn_i to an acceptor level of neutral V_{Zn} [31]. The green emission at ~523 to 524 nm is attributed to radiative transition from conduction band to the edge of the acceptor levels of O_{Zn} caused by oxygen antisites (O_{Zn}) [31, 40]. The UV emission and reduced visible emission shows that the undoped and Mn doped ZnO NPs have a good crystal structure with fewer oxygen vacancies.

3.6 FT–IR analysis

FTIR spectra of pure and Mn doped ZnO nanoparticles are shown in Fig.9. FTIR spectra for all the samples are assigned at room temperature. The Zn–O stretching frequency observed at 539 cm^{-1} for pure ZnO which is shifted to lower frequency as 525 cm^{-1} for Mn = 0.01M, 525 cm^{-1} for Mn = 0.02M and 525 cm^{-1} for Mn = 0.03M. The C=O stretching bands at 1500-1650 and at 2344, 2330, 2358 cm^{-1} are arising from the absorption of atmospheric CO_2 [41]. The bands around 1200 and 1100 cm^{-1} are attributed to the characteristic frequency of inorganic ions. The additional bands are observed at 1406 cm^{-1}, due to the microstructural formation of the sample. The wide absorption peaks in the range of 3410–3465 cm^{-1}, related to the -OH group, may due to the water adsorbed on the surface of nanoparticles.

3.7 Antibacterial Properties

At present the nanoparticles are being extensively studied to antibacterial activity. Several factors such as reduced amount of toxicity level and heat resistance are accountable for the use of NPs in the biological applications [42, 43]. The pure and Mn doped ZnO nanoparticles are investigated with respect to potential antimicrobial applications. The microbial sensitivity to the nanoparticles is found to vary depending on the microbial species and also due to ZnO and Mn concentrations. The bactericidal effect of the nanoparticles of pure and Mn doped ZnO is tested against harmful micro organisms. The two tested concentrations of 0.6 and 1.20 mg/disk produce zone of inhibition. The antimicrobial activity

of pure and Mn doped ZnO is scrutinized with two micro organisms (*S. epidermidis* & *P. aeruginosa*) using the disk diffusion test.

Figs. 10 (a) and (b) show the development of antibacterial activity of pure ZnO and Mn doped ZnO NPs. ZnO and Mn doped ZnO NPs exhibit antibacterial activity as shown in Figs. 9 (a) and (b). As said earlier, the higher ROS is generally produced to the decreasing particles size, larger surface area, diffusion ability of the reactant molecules and increase in oxygen vacancies. In present work, the antimicrobial activity of the ZnO NPs is essentially attributed to the combination of several factors such as ROS, and the release of Zn^{2+}.

The above mechanism of light induced generation of ROS can be given in equation form as following [43],

$$ZnO + h\upsilon \rightarrow e^- + h^+$$

$$h^+ + H_2O \rightarrow OH + H^+$$

$$e^- + O_2 \rightarrow \bullet O_2^-$$

$$\bullet O_2^- + H^+ \rightarrow HO_2\bullet$$

$$HO_2 \bullet + H^+ \rightarrow H_2O_2$$

From the result of photoluminescence studies for ZnO and Mn doped ZnO NPs, the violet and blue-green emissions can have the possibility of interstitial incorporation of Mn and Zn ions into the ZnO lattice. The second reason for the antibacterial activity is that when Zn^{2+} released by ZnO contacts with the cell membranes of microbe, the cell membranes with negative electricity and $Zn^{2+}$with positive electricity attract mutually and then the Zn^{2+} would penetrate into the cell membranes and react with sulfhydryl inside the cell membranes. As a result, the activity of synthetase in the microbe is so damaged that the cells lose the ability of division growth, which leads to death of the microbe.

Moreover, the antimicrobial activity and unreleased of Mn^{2+} ions cannot be accountable for the biocide activity of the Mn doped sample. But the replacement of Mn in the Zn site enhanced the photoactivity of the particles as related to ZnO NPs because of the similarity in ionic radii between Mn^{2+} (0.66 Å) and Zn^{2+} (0.74 Å). From the PL spectra of pure and Mn doped ZnO, the wavelengths of green emissions are at 523 and 524 nm. These indications increased the oxygen vacancies in the Mn doped ZnO NPs leading to more ROS as compared to that of ZnO NPs.

The NPs with uneven surfaces and rough edges have adhered to the bacterial wall and these causes damage to the cell membrane [44]. From the flied emission scanning electron microscopy (FESEM) image, the Mn doped ZnO NPs have uneven ridges and cluster formations at their outer surface leading to antibacterial activity.

Normally, bactericidal agents are potential to inhibit in the clinical field because bactericides lead to rapid and better recovery from the bacterial infection and such as minimize the risk of the emergence of drug resistance [45].

Interestingly in the present study the zone of inhibition reflects the degree of susceptibility of the microorganism. The strains incorporated to the disinfectants exhibit larger inhibition zone, whereas resistant strains exhibit smaller inhibition zone (see Fig.11). All the bacterial strains depict higher sensitivity to the higher concentration (1.2 mg/ml) for both Pure ZnO and Mn doped ZnO NPs. When compared to the positive control Methicillin (10mg/ml), except *S. epidermis,* it exhibits larger zone of inhibition than the positive control at pure ZnO and Mn doped ZnO NPs.

3. 8 Magnetic properties

The influence of pure and Mn doped ZnO NPs on the magnetic properties are studied. The undoped ZnO NPs is existence with diamagnetic behaviour at magnetic moment 0.0096

emu/g and also observed that the magnetic moment (0.00809, 0.0304 and 0.0408 emu/g) of Mn doped ZnO NPs increased with the increase of Mn doping concentration (Fig. 12). The alterations in the M–H loop has been described based on the magnetic contribution from the alignment of strong exchange interaction in *d–d* couple with manganese ion concentration in the BMP model, suggesting that the Mn^{2+} ion contributes to the ferromagnetism of Mn-doped ZnO nanoparticles [6,44]. The strain was increased significantly with the addition of antiferromagnetic Mn^{2+}. At high Mn concentrations the strain is notably high and accompanies the RTFM. Increase of Mn doping concentration enhances the linear behaviour of the M-H loop. In 1%, 2% and 3% Mn doped ZnO NPs, there is no formation of a strong ferromagnetic coupling among the transition metal cations (Mn^{2+}) at the microscopic level. Hence, the possibility of strong ferromagnetic behaviour of Mn doped ZnO is ruled out, but it results to the weak ferromagnetic or super-paramagnetic behaviour.

4. Conclusion

The pure ZnO and Mn doped ZnO NPs were synthesized by the co-precipitation method. The X-ray diffraction (XRD) results confirmed that the synthesized NPs formed with hexagonal wurtzite structure. The HRTEM images of the synthesized NPs showed nanospheres morphology and a reduction in the particle size with respect to the Mn concentrations. The bandgap of ZnO NPs was increased from 2.7 to 2.9 eV upon Mn doping. The antibacterial studies were performed against a set of bacterial strains. Among them, *Staphylococcus epidermidis* showed the higher sensitivity to Mn doped ZnO nanoparticles which were powerful than the positive control and *Pseudomonas aeruginosa* strain was less sensitive to NPs.

Declarations

Funding – Not Applicable

Conflicts of interest/Competing interests: Authors declared no conflict of interest

Availability of data and material - Not Applicable

Code availability- Not Applicable

Additional declarations for articles in life science journals that report the results of studies involving humans and/or animals - Not Applicable

Ethics approval- Not Applicable

References

1. R. D. Handy, F. Von der Kammer, J. R. Lead, M. Hassellöv, R. Owen, M. Crane, *Ecotoxicology*, *17*, 287 (2008).
2. N.M. Franklin, N.J. Rogers, S.C. Apte, G.E. Batley, G.E. Gadd, P.S. Casey, *Environ. Sci Tech*, *41*, 8484 (2007).
3. Y. Liu, L. He, A.Mustapha, L. Hi, Z. Q. Hu, M. Lin, *J. Appl. Microbio*, *107*, 1193 (2009).
4. S. Singh, M.R. Rao, *Phys. Rev B*, *80*, 045210(2009).
5. J. Alaria, P. Turek, M. Bernard, M. Bouloudenine, A. Berbadj, N. Brihi, A. Dinia, *Chem Phys Lett*, *415*, 337 (2005).
6. V. Gandhi, R. Ganesan, H.H. Abdulrahman Syedahamed, M. Thaiyan, *J Phys Chem C*, *118*, 9715 (2014).
7. M.H. Sluiter, Y. Kawazoe, P. Sharma, A. Inoue, A. Raju, C. Rout, U.V. Waghmare, *Phys Rev Lett*, *94*, 187204 (2005).
8. L. Hsu, C.S. Yeh, C.C. Kuo, B.R. Huang, S. Dhar, *J. Optoelectronics Advan Mater*, *7*, 3039 (2005).
9. R.N. Bhargava, D. Haranath, A. Mehta, *J Korean Phys. Soc*, *53*, 2847 (2008).
10. S.Y. Bae, C.W. Na, J.H. Kang, J. Park, *J Phys Chem B*, *109*, 2526 (2005).
11. I. Djerdj, Z. Jagličić, D. Arčon, M. Niederberger, *Nanoscale*, *2*, 1096 (2010).
12. I. Djerdj, G. Garnweitner, D. Arčon, M. Pregelj, Z. Jagličić, M. Niederberger, *J Mater Chem*, *18*, 5208 (2008).
13. S.I. Hirano, *American Ceram Soc Bulletin*, *66*, 1342 (1987).
14. D. Vorkapic, T. Matsoukas, T. *J Amer. Ceram. Soc*, *81*, 2815 (1998).
15. P.S. Patel, M.V. Hathi, *J. Chem. Pharm. Res*, *2*, 78 (2010)
16. S.S. Cetin, I. Uslu, A. Aytimur, S. Ozcelik, *Ceram Inter*, *38*, 4201 (2012).

17. B. Karthikeyan, T. Pandiyarajan, K. Mangaiyarkarasi, *Spectrochimica Acta Part A:*, *82*, 97 (2011).
18. R. Brayner, R. Ferrari-Iliou, N. Brivois, S. Djediat, M.F. Benedetti, F. Fiévet, *Nano lett*, *6*, 866 (2006).
19. M. Li, L. Zhu, D. Lin, *Environ. Sci Techn*, *45*, 1977 (2011).
20. N. Talebian, S.M. Amininezhad, M. Doudi, *J. Photochem Photobio B: Biology*, *120*, 66 (2013).
21. G.X. Tong, F.F. Du, Y. Liang, Q. Hu, R.N. Wu, J.G. Guan, X. Hu, *J. Mater. Chem B*, *1*, 454 (2013).
22. G. Vijayaprasath, R. Murugan, S. Palanisamy, N.M Prabhu, T. Mahalingam, Y. Hayakawa, G. Ravi, *J. Mater. Sci: Mater. Electron*, *26*, 7564 (2015).
23. H.A. Foster, I.B. Ditta, S. Varghese, A. Steele, *Appl Microbio Biotechn*, *90*, 1847 (2011).
24. B. Staumal, B. Baretzky, A. Mazilkin, S.Protasava, A. Petrastraumal, J. European Ceramic Soc JECS 29, 1963 (2009)
25. Suryanarayana, C., & Norton, M. G. *X-ray diffraction: a practical approach*. Springer Science & Business Media (2013).
26. P. Singh, A. Kaushal, D. Kaur, *J. Alloys Compd*, *471*, 11 (2009).
27. S. Suwanboon, T. Ratana, T. Ratana, J. *Walailak J. Sci. Techn (WJST)*, *4*, 111 (2007).
28. M. Vafaee, M.S. Ghamsari, *Mater Lett*, *61*, 3265 (2007).
29. W. Xie, X. Huang, *Cataly Lett*, *107*, 53 (2006).
30. A. Hernández, L.Maya, E. Sánchez-Mora, E.M. Sánchez, *J. Sol-Gel Sci. Tech*, *42*, 71 (2007).
31. S.K. Mishra, R.K. Srivastava, S.G. Prakash, *J. Alloys Compd*, *539*, 1 (2012).
32. S.K. Mishra, R.K. Srivastava, S.G. Prakash, R.S. Yadav, A.C. Panday, *Opto-Electronics Rev*, *18*, 467 (2010).
33. K. Vanheusden, W.L. Warren, C.H. Seager, D.R. Tallant, J.A. Voigt, B.E Gnade, *J. Appl Phys*, *79*, 7983 (1996).
34. Z.M. Liao, H.Z. Zhang, Y.B. Zhou, J. Xu, J.M. Zhang, D.P. Yu, *Phys Lett A*, *372*, 4505 (2008).
35. J.C. Johnson, K.P. Knutsen, K. P H. Yan, M. Law, Y. Zhang, P. Yang, R.J. Saykally, *Nano Lett*, *4*, 197 (2004).
36. Z. Fan, P.C. Chang, J.G. Lu, E.C. Walter, R.M. Penner, C.H. Lin, H. P. Lee, *Appl phy lett*, *85*, 6128 (2004).

37. L. Wischmeier, C. Bekeny, T. Voss, S. Börner, W. Schade, W. *physica status solidi (b)*, *243*, 919 (2006).
38. I. Shalish, H. Temkin, V. Narayanamurti, *Phys Rev B*, *69*, 245401 (2004).
39. J. Grabowska, A.Meaney, K. K.Nanda, J.P. Mosnier, M.O. Henry, J.R. Duclère, E. McGlynn, *Phys Rev B*, *71*, 115439 (2005).
40. J. Wang, L. Gao, *J. Mater Chem*, *13*, 2551-2554 (2003).
41. C. F.Jin, X.Yuan, W. W.Ge, J. M. Hong, X. Q. Xin, *Nanotech*, *14*, 667 (2003).
42. S. B. Qadri, E. F. Skelton, D. Hsu, A.D. Dinsmore, J. Yang, H. F. Gray, B.R. Ratna, *Phys Rev B*, *60*, 9191 (1999).
43. R. Prasad, G. Rattan, *Bulletin of Chemical Reaction Engineering & Catalysis*, *5*, 7 (2010).
44. R. Brayner, R. Ferrari-Iliou, N.Brivois, S.Djediat, M. F. Benedetti, F. Fiévet, *Nano lett*, *6*, 866 (2006).
45. G. Vijayaprasath, R. Murugan, S. Palanisamy, N.M. Prabhu, T. Mahalingam, Y. Hayakawa, G. Ravi, Mater Res Bullet., 76, 48 (2016)
46. G. L. French, *J. Antimicrobial Chemotherapy*, *58*, 1107 (2006).

Figure captions

Fig. 1: X-ray diffraction patterns of pure ZnO, ZnMnO1, ZnMnO2, ZnMnO3 samples.

Fig. 2 (a): Variation of lattice parameters 'a' and 'c' with Mn concentrations. **(b)** Variation of unit cell volume and bond length with Mn concentration

Fig. 3. (a): The W–H analysis of pure and Mn doped ZnO nanoparticles (b) Variation of microstrain along with the Mn concentrations

Fig. 4.1 (a-d): HRTEM images and SAED pattern of Pure ZnO Nanoparticles.

Fig. 4.2 (a-d): HRTEM images and SAED pattern of (ZnMnO2) Mn doped ZnO Nanoparticles

Fig. 5 (a-d): EDAX spectrum for pure ZnO and different concentration of Mn doped ZnO nanoparticles.

Fig. 6: UV absorption spectra of pure ZnO and different Mn concentration of ZnO nanoparticles.

Fig. 7: Shows band gap energy of ZnO and Mn doped ZnO Nanoparticles

Fig.8: **(a)** Lorentzian decomposed photoluminescence spectra of ZnO and Mn doped ZnO nanoparticles and **(b)** variation in the UV peak position with respect to the Mn concentrations

Fig .9: FTIR spectra of ZnO and Mn doped ZnO Nanoparticles

Fig. 10: The zone of inhibition formed around each disc, loaded with test samples indicated the antimicrobial activity of (a) *Staphylococcus epidermidis* and (b) *Pseudomonas aeruginosa.*

Fig. 11: The zone of inhibition formed around each disc, loaded with test samples indicated the antibacterial activity of (a) *S. Epidermis* and (b) *P. aeruginosa*.

Fig. 12: Magnetization curves loops for ZnO and Mn doped ZnO Nanoparticles

Table -1. Sample coding and Sample composition:

S.no	Sample Coding	Sample Composition
1.	**Pure ZnO (Zn-100%)**	0.100 M Zn $(CH_3COO)_2.H_2O$ + 0.8 M NaOH
2.	**ZnMnO1 (Zn- 99% & Mn-1%)**	0.099 M Zn $(CH_3COO)_2.H_2O$ + 0.8 M NaOH + 0.001 M Mn $(CH_3COO)_2.H_2O$
3.	**ZnMnO2 (Zn- 98% & Mn-2%)**	0.098 M Zn $(CH_3COO)_2.H_2O$ + 0.8 M NaOH + 0.002 M Mn $(CH_3COO)_2.H_2O$
4.	**ZnMnO3 (Zn- 97% & Mn-3%)**	0.097 M Zn $(CH_3COO)_2.H_2O$ + 0.8 M NaOH + 0.003 M Mn $(CH_3COO)_2.H_2O$

Table-2. **Particle size and lattice parameter values of ZnO and Mn doped ZnO Nanoparticles**

Samples	Particle size (nm)	a (Å)	c (Å)
Pure ZnO	41.8	3.2438	5.1985
ZnMnO1	41.2	3.3038	5.2857
ZnMnO2	40.1	3.3027	5.2847
ZnMnO3	33.8	3.3074	5.2940

Table-3. Compositional analysis of ZnO and ZnMnO NPs

Sample	Dopant concentration	Experimental results (Atomic %)		
		Zn	Mn	O
ZnO	0	59.25	-	40.75
ZnMnO1	1	40.22	0.53	59.25
ZnMnO2	2	44.81	1.04	54.15
ZnMnO3	3	40.60	1.91	57.48

Figures

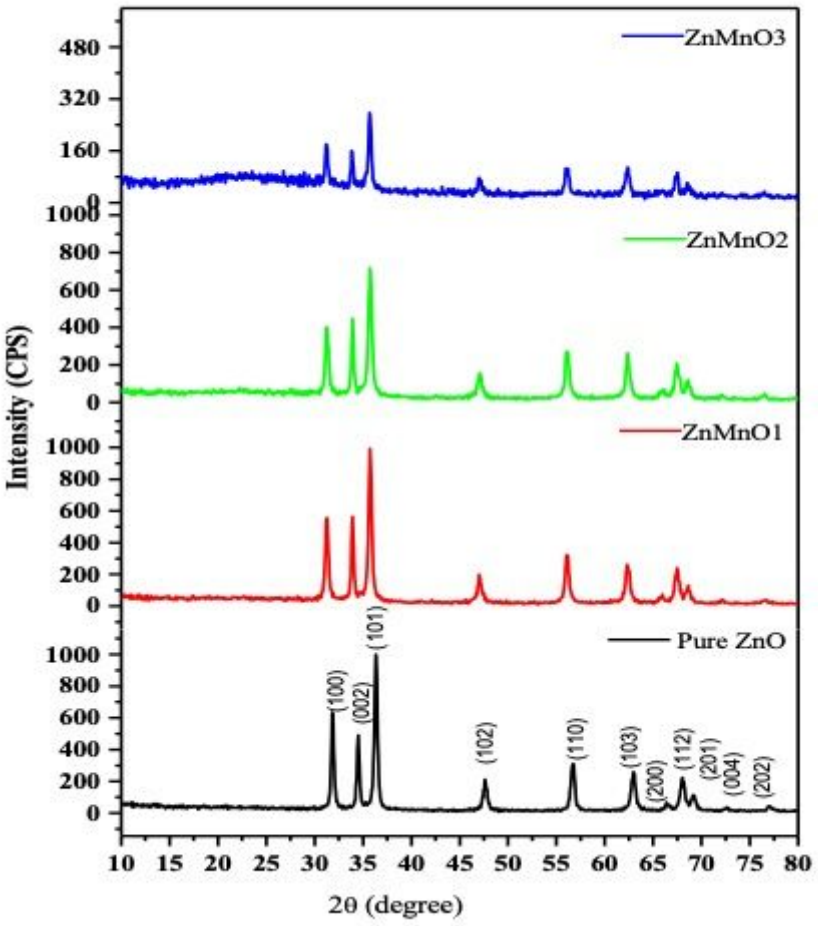

Figure 1

X-ray diffraction patterns of pure ZnO, ZnMnO1, ZnMnO2, ZnMnO3 samples.

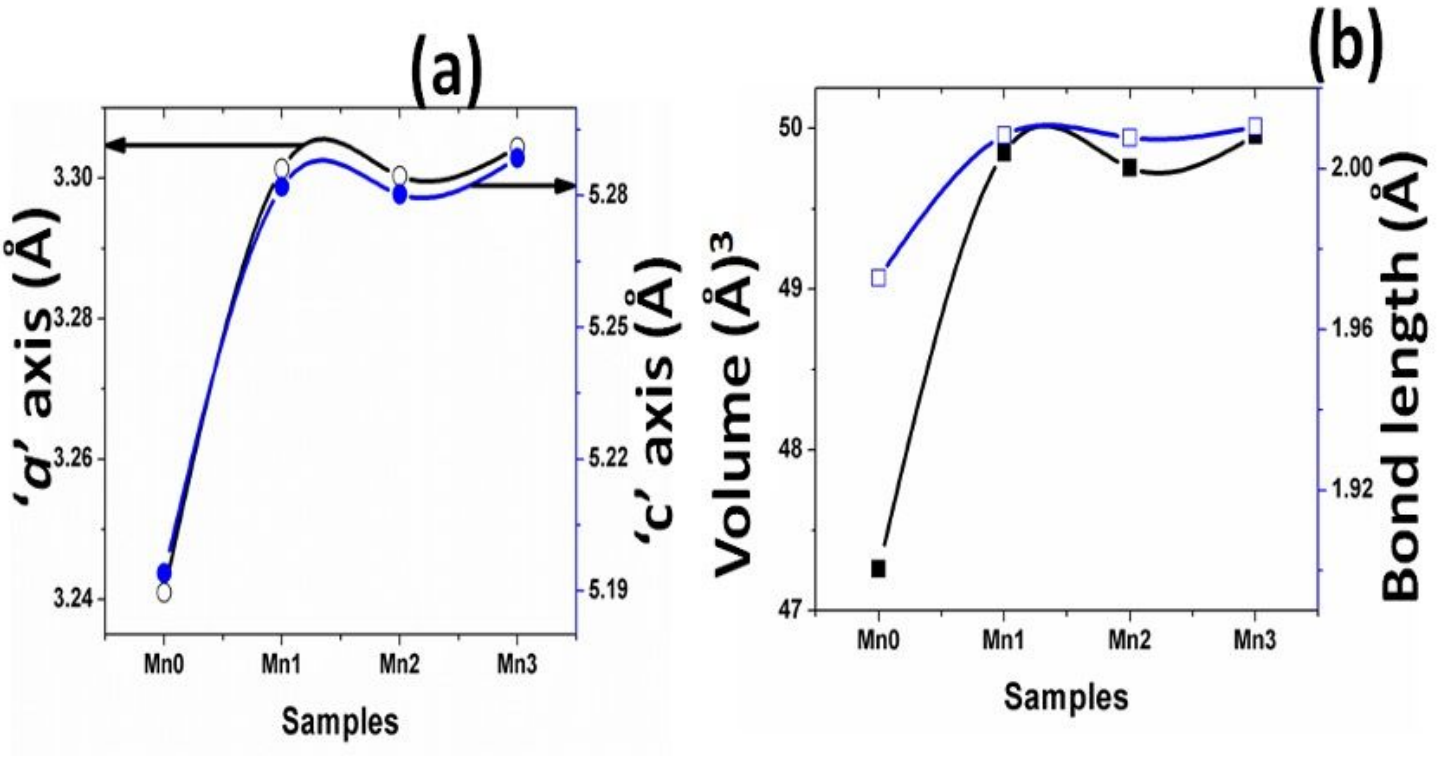

Figure 2

(a): Variation of lattice parameters 'a' and 'c' with Mn concentrations. (b) Variation of unit cell volume and bond length with Mn concentration

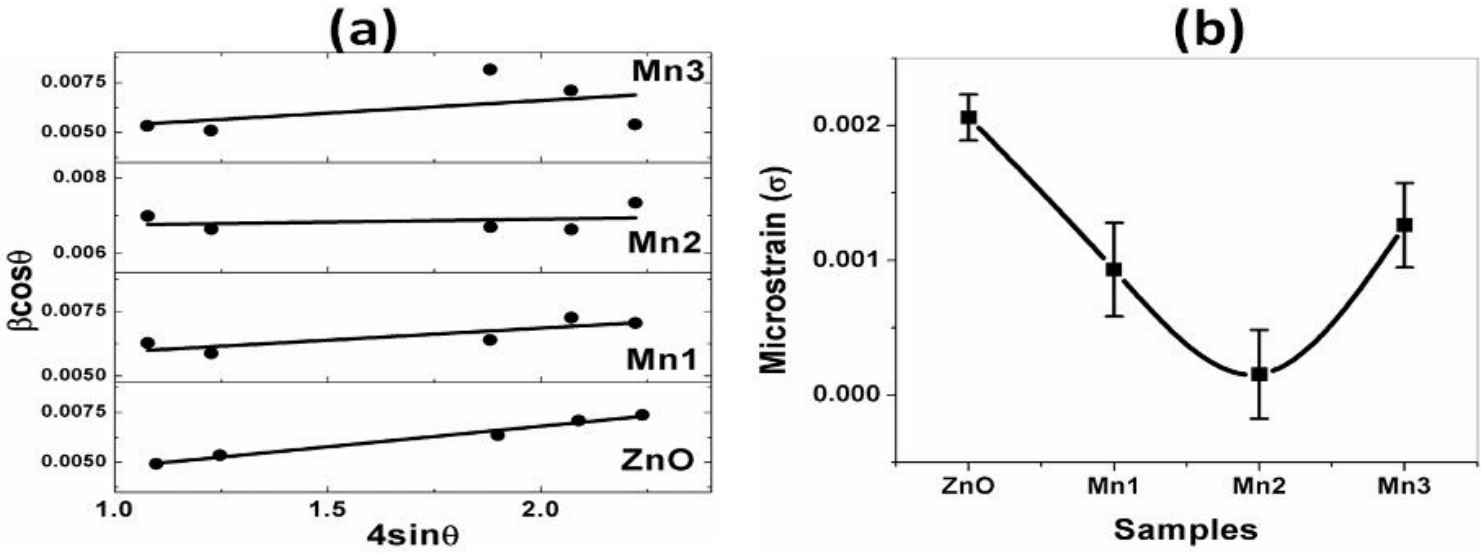

Figure 3

(a): The W–H analysis of pure and Mn doped ZnO nanoparticles (b) Variation of microstrain along with the Mn concentrations

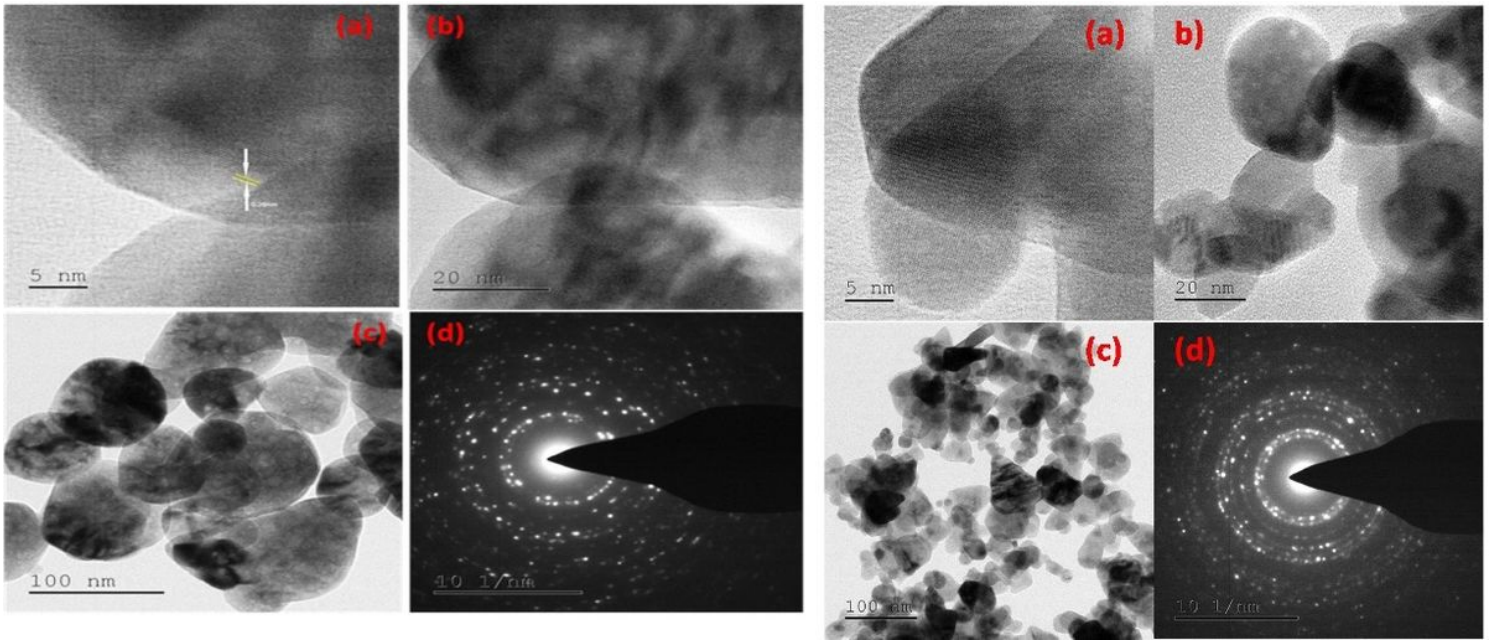

Figure 4

(a-d): HRTEM images and SAED pattern of Pure ZnO Nanoparticles. (a-d): HRTEM images and SAED pattern of (ZnMnO2) Mn doped ZnO Nanoparticles

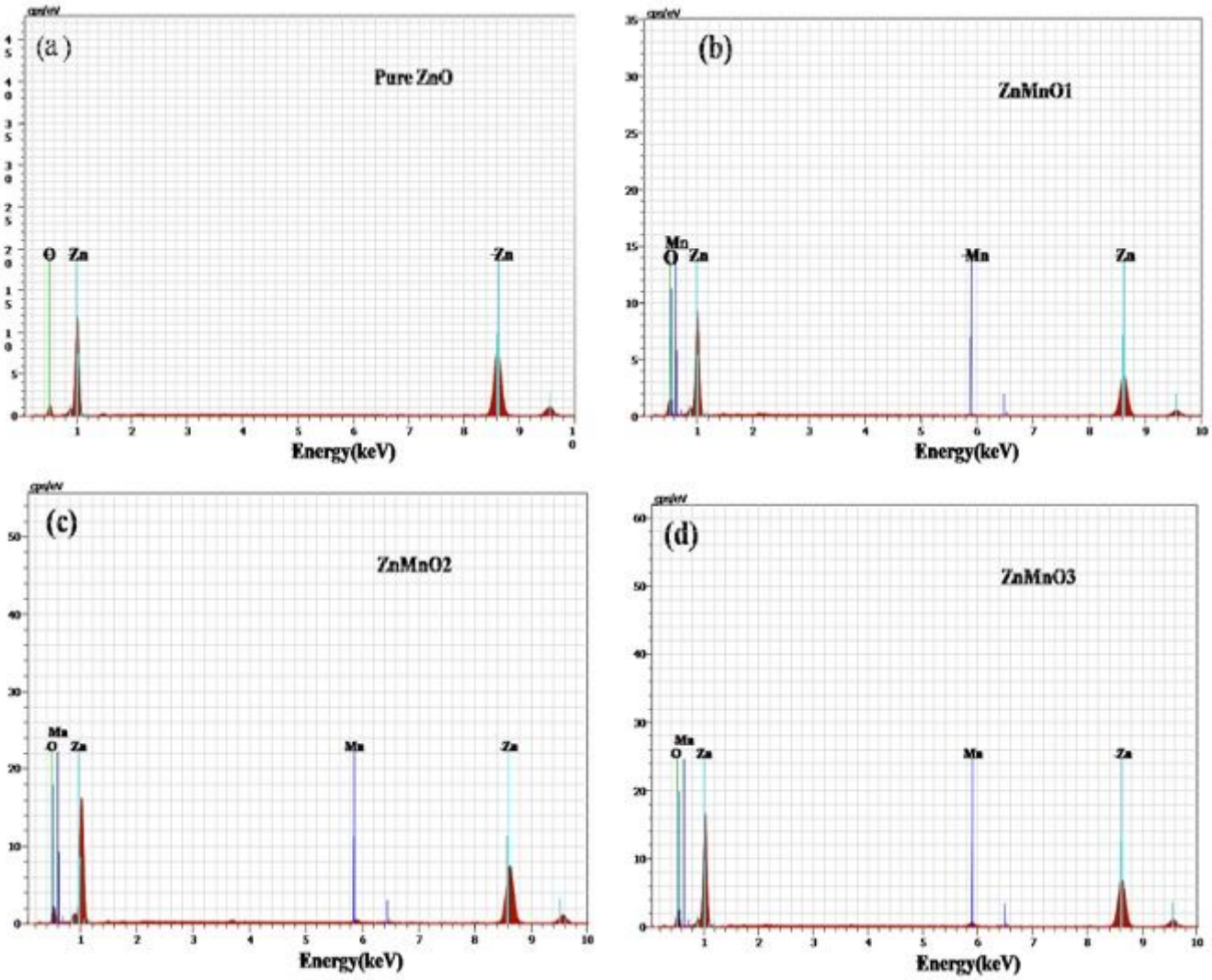

Figure 5

(a-d): EDAX spectrum for pure ZnO and different concentration of Mn doped ZnO nanoparticles.

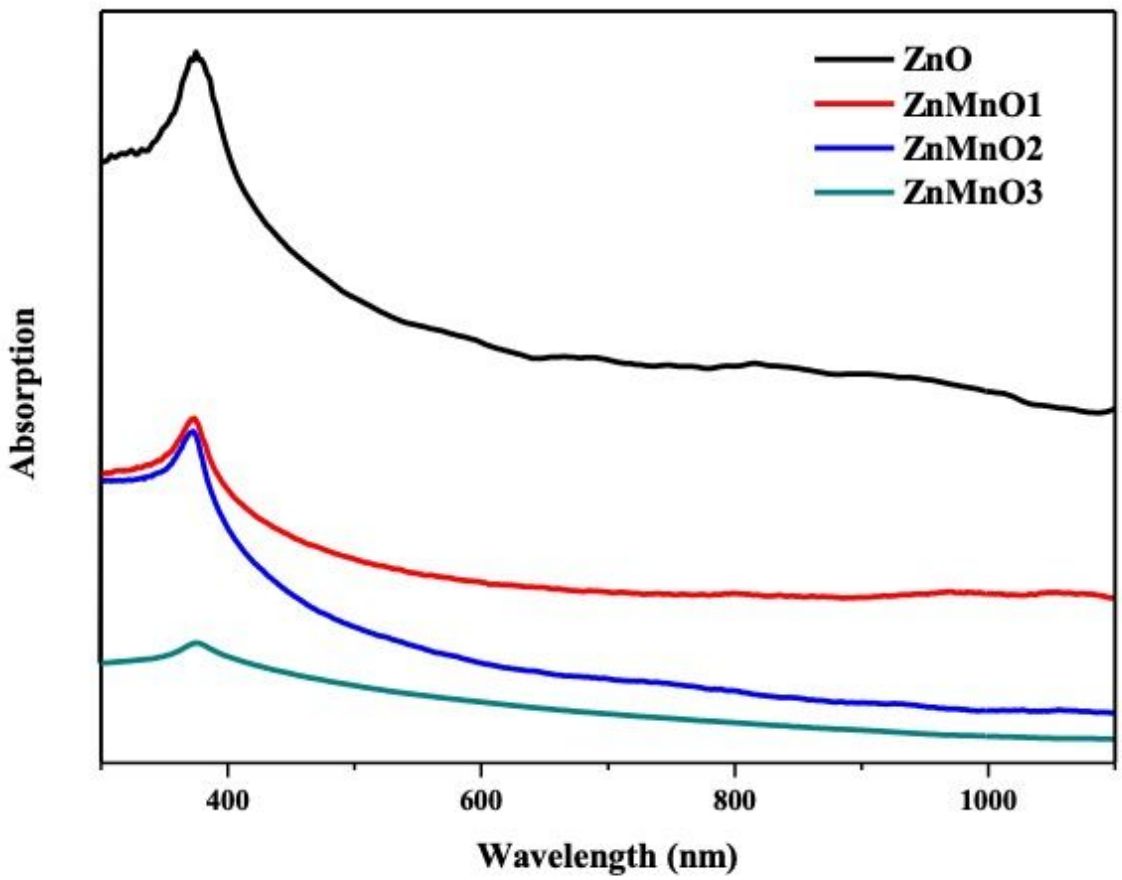

Figure 6

UV absorption spectra of pure ZnO and different Mn concentration of ZnO nanoparticles.

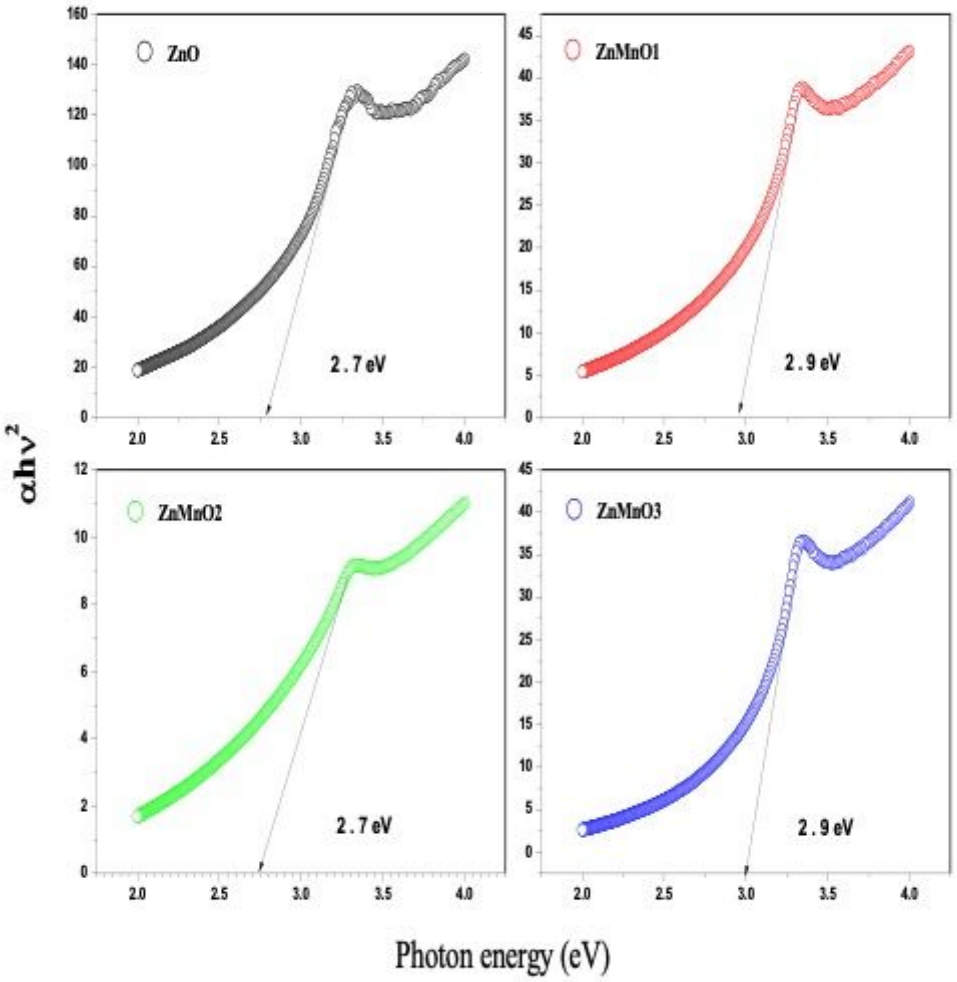

Figure 7

Shows band gap energy of ZnO and Mn doped ZnO Nanoparticles

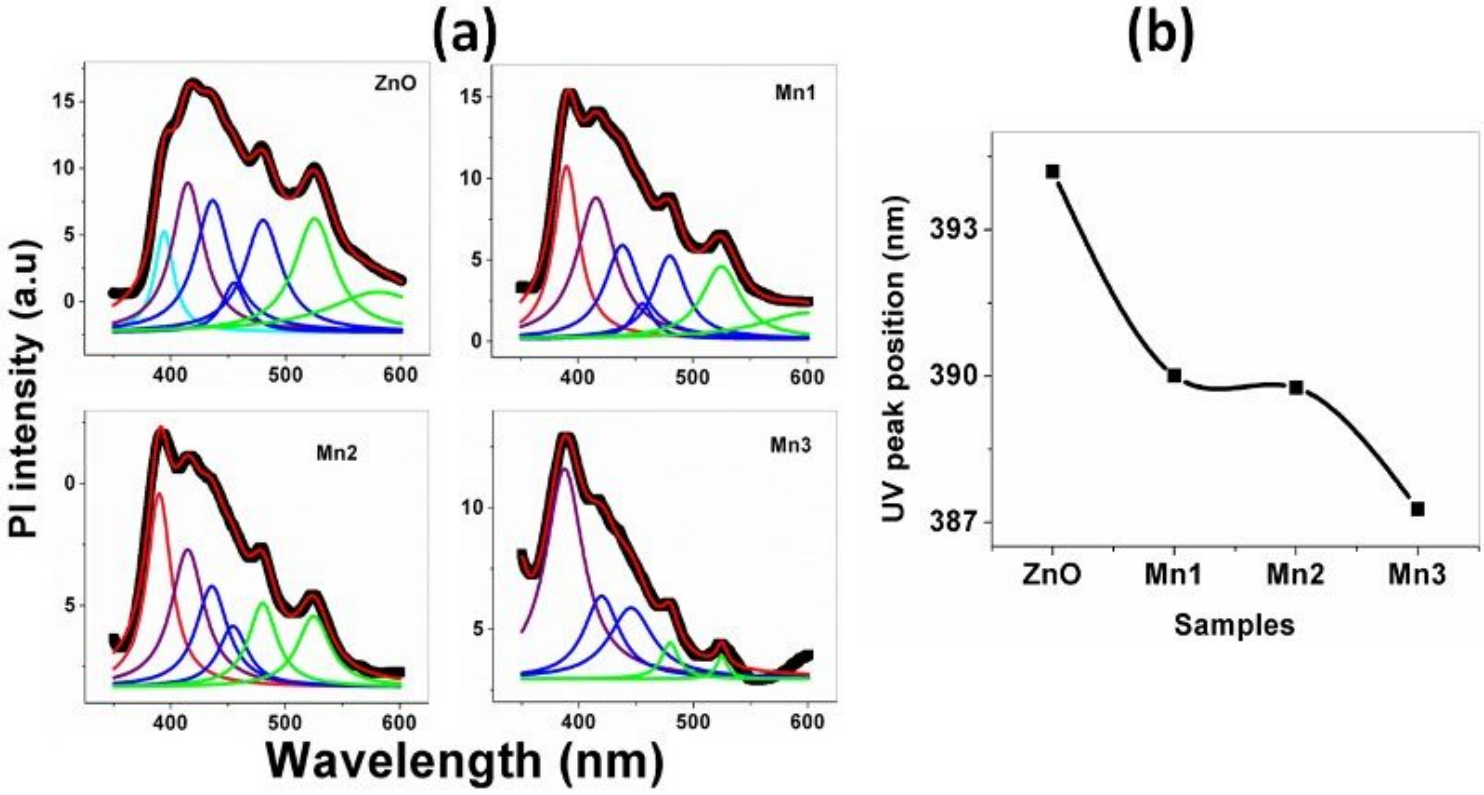

Figure 8

(a) Lorentzian decomposed photoluminescence spectra of ZnO and Mn doped ZnO nanoparticles and (b) variation in the UV peak position with respect to the Mn concentrations

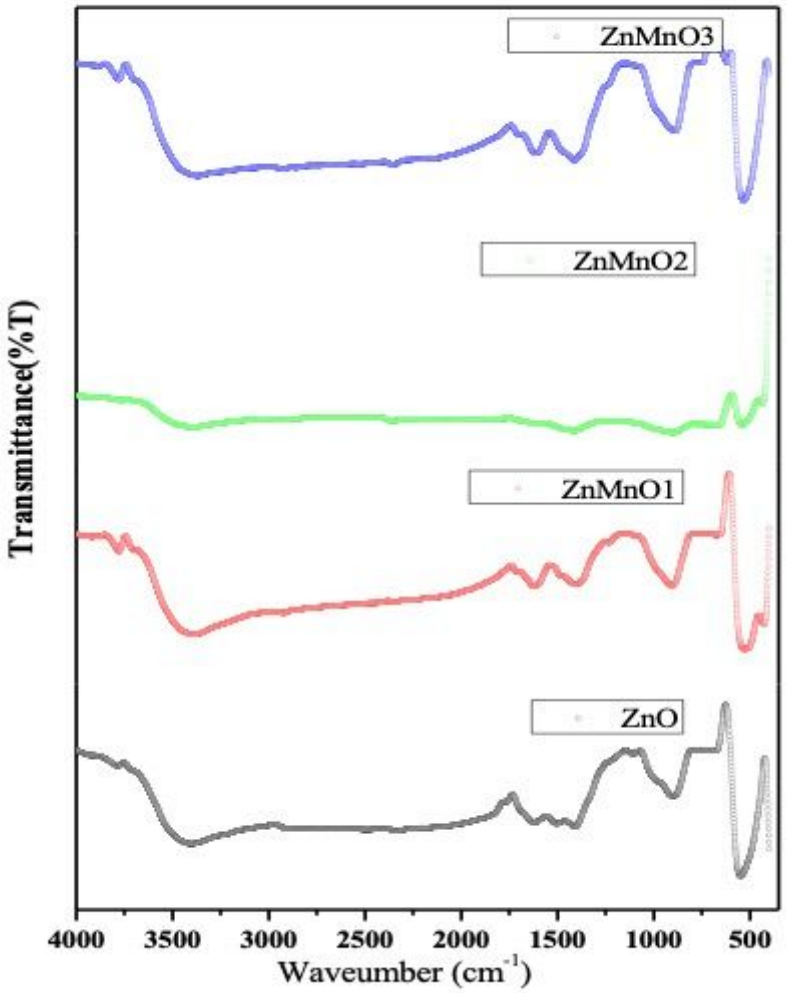

Figure 9

FTIR spectra of ZnO and Mn doped ZnO Nanoparticles

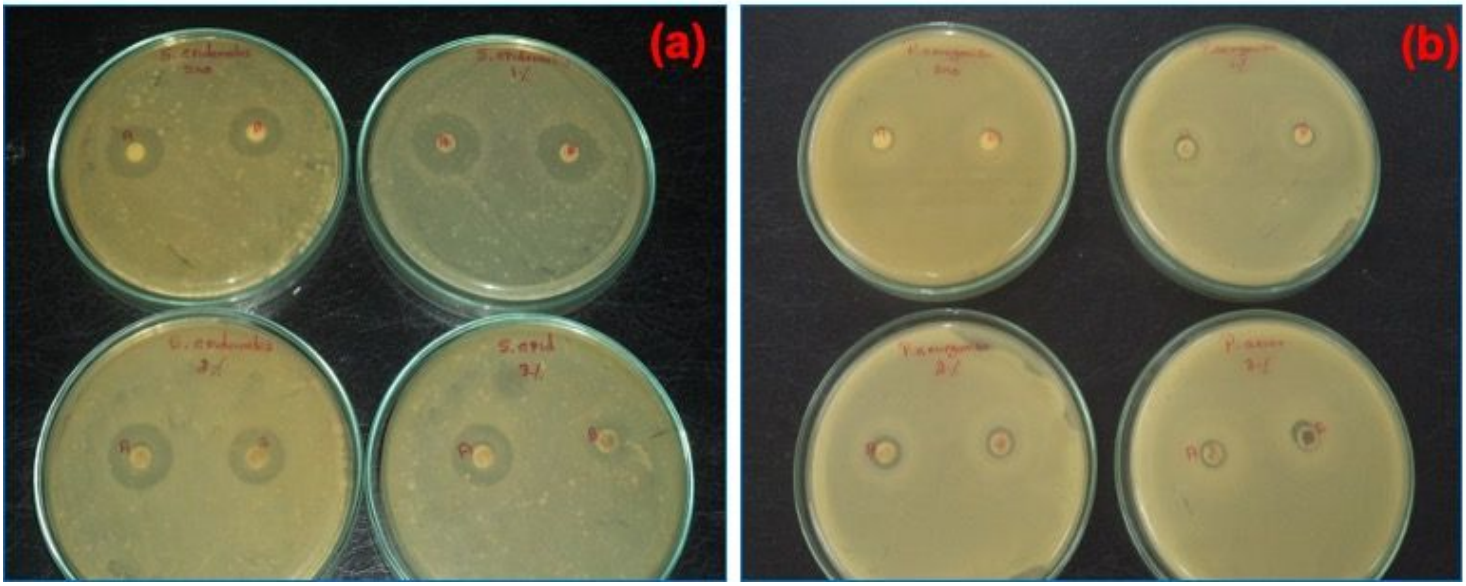

Figure 10

The zone of inhibition formed around each disc, loaded with test samples indicated the antimicrobial activity of (a) Staphylococcus epidermidis and (b) Pseudomonas aeruginosa.

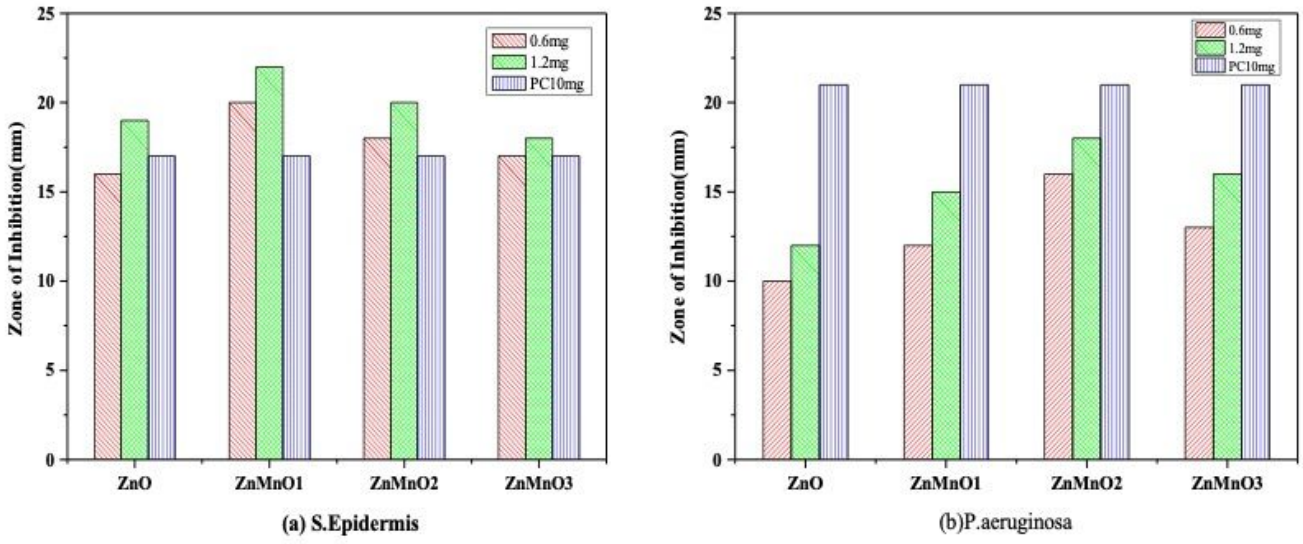

Figure 11

The zone of inhibition formed around each disc, loaded with test samples indicated the antibacterial activity of (a) S. Epidermis and (b) P. aeruginosa.

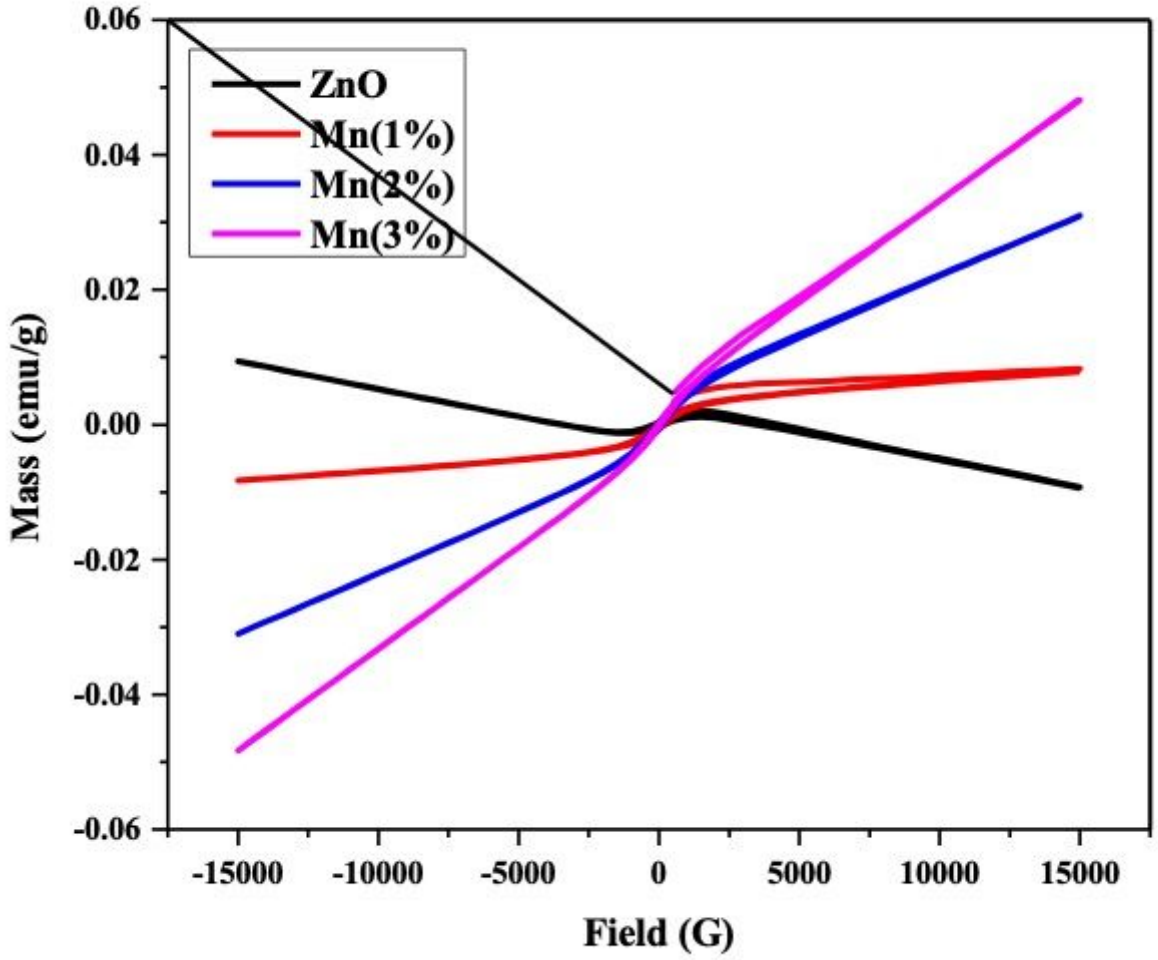

Figure 12

Magnetization curves loops for ZnO and Mn doped ZnO Nanoparticles